



ELSEVIER

Computer Physics Communications 87 (1995) 253–265

Computer Physics
Communications

Simulations of brittle solids using smooth particle hydrodynamics

W. Benz ^{a,1}, E. Asphaug ^{b,2}

^a *Steward Observatory and Lunar and Planetary Laboratory, University of Arizona, Tucson, AZ, 85721, USA*

^b *NASA Ames Research Center, MS 245-3, Moffett Field, CA, 94035, USA*

Received 19 May 1994; revised 31 August 1994

Abstract

We describe a version of the smooth particle hydrodynamics (SPH) method suitable for modeling solids. The model includes strength and implements a von Mises yielding relation for stresses beyond the Hugoniot elastic limit. At lower stresses associated with brittle failure we use a rate-dependent strength based on the nucleation and growth of explicit Weibull flaws. We illustrate the capabilities of our fracture model by examining the propagation of cracks in a simple tensile rod, and by comparing simulations with laboratory experiments for high speed impacts and cratering.

1. Introduction

Fracture depends on the entire stress history of a given piece of material. A Lagrangian approach, in which the frame of reference is attached to the material, is therefore the natural framework for solving these equations; Eulerian codes have great difficulties of following accurately stress history and the development of cracks. Conventional Lagrangian codes, however, are unable to handle large material deformations, as tangling and deformation of the grid severely affect the accuracy of derivatives.

Smooth particle hydrodynamics (Lucy 1977, Benz 1990, Monaghan 1992) does not suffer from this problem. The hydrodynamical quantities

(pressure, density, velocity, etc.) in SPH are known at a finite number of points, called particles, which move with the flow. Given any spatial distribution of these points, the SPH technique allows the computation of spatial derivatives without an underlying grid. Once the spatial derivatives have been computed and forces determined, time integration proceeds in the usual way. Thus, SPH provides an interesting alternative to traditional grid-based methods, differing widely not only on a purely conceptual level, but also on numerical requirements and hence on algorithms necessary to make the method efficient on a specified machine architecture.

Over the past few years, SPH has been extended to the simulations of solids (Liberky and Petschek 1990, Wingate and Fisher 1993, Benz and Asphaug 1994) by including the non-diagonal terms of the stress tensor (using Hooke's law) modified by a von Mises yielding relation for

¹ E-mail: wbenz@as.arizona.edu.

² E-mail: asphaug@cosmic.arc.nasa.gov.

stresses beyond the elastic limit. At the lower stresses associated with brittle failure, we developed a new fracture model based on the nucleation of incipient flaws whose number density is given by a Weibull distribution. We begin this paper with a review of the basic equations describing the dynamics of brittle solids (Sections 2 and 3). In Section 4 we discuss the detailed implementation of these equations into the SPH framework. To identify the strengths and weaknesses of our method, we have begun a comprehensive testing campaign, applying our code to the simulation of well documented laboratory experiments ranging from small-scale impacts and disruptions to high-yield explosions and nuclear craters. We present selected results from these tests in Section 5.

2. Equations for an elastic–perfectly plastic strength model

The equations to be solved are the well-known conservation equations of hydrodynamics and can be found in most standard textbooks. We follow here previous papers on the subject (Liberky and Petschek 1990, Wingate and Fisher 1991) and assume a basic Hooke's law model in which the stress deviator rate is proportional to the strain rate.

The first equation describes mass conservation and is written in the following manner:

$$\frac{d\rho}{dt} + \rho \frac{\partial}{\partial x^\alpha} v^\alpha = 0, \quad (1)$$

where d/dt is the Lagrangian time derivative. The other variables have their usual meaning. We also assume the usual summation rule over repeated indices. The next equation describes the conservation of momentum (no gravity):

$$\frac{dv^\alpha}{dt} = \frac{1}{\rho} \frac{\partial}{\partial x^\beta} \sigma^{\alpha\beta}, \quad (2)$$

where $\sigma^{\alpha\beta}$ is the stress tensor given by

$$\sigma^{\alpha\beta} = -P\delta^{\alpha\beta} + S^{\alpha\beta}, \quad (3)$$

where P is the pressure and $S^{\alpha\beta}$ the traceless deviatoric stress tensor and $\delta^{\alpha\beta}$ the Kronecker

symbol. Finally, the conservation of energy is given by the equation

$$\frac{du}{dt} = -\frac{P}{\rho} \frac{\partial}{\partial x^\alpha} v^\alpha + \frac{1}{\rho} S^{\alpha\beta} \dot{\epsilon}^{\alpha\beta}, \quad (4)$$

where $\dot{\epsilon}^{\alpha\beta}$ is the strain rate tensor given by

$$\dot{\epsilon}^{\alpha\beta} = \frac{1}{2} \left(\frac{\partial}{\partial x^\beta} v^\alpha + \frac{\partial}{\partial x^\alpha} v^\beta \right). \quad (5)$$

Contrary to fluid dynamics, this set of equations is not sufficient as the time evolution of $S^{\alpha\beta}$ still needs to be specified. In order to do so we adopt Hooke's law and write

$$\begin{aligned} \frac{dS^{\alpha\beta}}{dt} &= 2\mu \left(\dot{\epsilon}^{\alpha\beta} - \frac{1}{3} \delta^{\alpha\beta} \dot{\epsilon}^{\gamma\gamma} \right) \\ &\quad + \text{rotation terms,} \end{aligned} \quad (6)$$

where μ is the shear modulus. Rotation terms are needed to allow the transformation of the stresses from the reference frame associated with the material to the laboratory reference frame which all other equations are specified. The simplest possible implementation consists in writing the rotation terms as $-\mathbf{R}\boldsymbol{\sigma} + \boldsymbol{\sigma}\mathbf{R}$ with the rotation rate tensor $R^{\alpha\beta}$ written as

$$R^{\alpha\beta} = \frac{1}{2} \left(\frac{\partial}{\partial x^\beta} v^\alpha - \frac{\partial}{\partial x^\alpha} v^\beta \right). \quad (7)$$

This set of equations can now be solved provided we specify an equation of state, $P = P(\rho, u)$, and will describe perfectly elastic materials. It is well known, however, that actual materials are not perfectly elastic. A critical stress always exists, that, if applied to the material, results in permanent deformation. This "plastic" behavior can be introduced in the equations using the von Mises yielding criterion. We limit our deviatoric stress tensor by

$$S^{\alpha\beta} \Rightarrow f S^{\alpha\beta}, \quad (8)$$

where f is computed from

$$f = \min \left[\frac{Y_0^2}{3J_2}, 1 \right], \quad (9)$$

where J_2 is the the second invariant of the deviatoric stress tensor defined by

$$J_2 = \frac{1}{2} S^{\alpha\beta} S^{\alpha\beta} \quad (10)$$

and Y_0 is a material dependent yield stress which is in general $Y_0 = Y_0(T, \rho, \dots)$. For example, Y_0 decreases with increasing temperature, and beyond the melting point $Y_0 = 0$.

3. Fracture

In this section, we discuss various aspects of our fracture model which was originally derived from the continuum model of fragmentation developed by Grady and Kipp (1980). However, as shown by Benz and Asphaug (1994), their statistical model leads to inconsistencies between hydrodynamics and fragmentation unless the flaws are made explicit. Our model provides a hydrodynamically consistent mechanism for the existence and growth of explicit cracks.

We begin by assuming the existence of incipient flaws in brittle solids. We further assume that a probability distribution defines the most likely number of flaws per unit volume having failure strains lower than ϵ according to a power law

$$n(\epsilon) = k\epsilon^m \quad (11)$$

(Weibull 1939, Jaeger and Cook 1969). This Weibull distribution is isotropic, including no information about the location or orientation of any given flaw. The Weibull parameters m and k are material constants which can be determined from laboratory experiments, although data are still quite scarce. The coefficient k varies widely between various rock types, whereas the exponent m is typically between 6 and 12. Large values of m describe homogeneous rocks with uniform fracture thresholds, whereas rocks with small m have widely varying flaw strengths. It has been shown elsewhere (Melosh et al. 1992, Benz and Asphaug 1994) that m and k are not wholly independent constants, since rocks with equal $\ln(kV)/m$ tend to have similar overall disruption thresholds.

When a flaw becomes active (i.e. once the local tensile strain has reached the flaw's activation threshold) a crack is allowed to grow at a constant velocity c_g , which we set at 0.4 times the speed of a longitudinal elastic wave (Lawn and

Wilshaw 1975). The half-length of a growing crack is therefore

$$a = c_g(t - t'), \quad (12)$$

where t' is the crack activation time. To compute local stress-release due to the growth of cracks, we follow Grady and Kipp and introduce a state variable D ("damage"), $0 \leq D \leq 1$. Damage expresses the reduction in strength under tensile loading:

$$\sigma_D = \sigma(1 - D), \quad (13)$$

where σ is the elastic stress in the absence of damage and σ_D is the damage-relieved stress. A material with sufficient cracks to have a damage $D = 0.5$ feels half the stress it would otherwise feel under the same tensile strain. A fully damaged material is a cohesionless fluid, feeling no tensile or shear stress whatsoever.

As shown by Walsh (1965), a crack relieves stresses in a volume approximately equal to its circumscribing sphere. Thus, we define D locally as the fractional volume that is relieved of stress by local growing cracks

$$D = \frac{\frac{4}{3}\pi a^3}{V}, \quad (14)$$

where $V = \frac{4}{3}\pi R_s^3$ is the volume in which a crack of half-length R_s is growing. Using Eq. (12), we obtain a convenient differential equation for damage growth

$$\frac{dD^{1/3}}{dt} = \frac{c_g}{R_s}. \quad (15)$$

This equation expresses the evolution of D in a small subvolume of radius R_s of material subject to tensile strains. The overall damage experienced by the material under consideration is given by the distribution of D over the entire object. In an elemental subvolume V , damage is independent of strain once the activation threshold has been exceeded. However, over a larger volume it is not, since the number of active flaws are strain-dependent (Eq. (11)). In Subsection 4.3 (below) we describe how a single computational volume contains many elemental subvolumes, so that damage is in fact strain-dependent.

4. Smooth particle implementation

In this section, we discuss how the above equations are cast in the SPH framework. As many extensive reviews already exist in the literature (see for example Benz 1990, Monaghan 1992) we limit ourselves to the specifics pertaining to finite strength models. While the fracture model derived in the previous section may be implemented in any Lagrangian finite-difference hydrocode, SPH provides a very natural framework which is highly suitable to the propagation of fractures and the formation of fragments.

The additions to the SPH technique described here add a significant burden both in complexity and in computational requirements to the more familiar “perfect gas” version of the technique. For example, a particle is described by 17 variables: three positions, three velocities, density, energy, the smoothing length, the mass, the five components of the deviatoric stress tensor, damage and activation thresholds. Only the first 10 are needed for the simulation of fluids.

4.1. Elastic–perfectly plastic regime

We begin with mass conservation. We use the actual continuity equation to obtain the time-dependent value of the density rather than the usual weighted sum over neighbors. The expression we adopt for the SPH analog of Eq. (1) is

$$\frac{d\rho_i}{dt} = - \sum_{j=1}^N m_j (v_j^\alpha - v_i^\alpha) \frac{\partial W_{ij}}{\partial x_i^\alpha}, \quad (16)$$

where W_{ij} is the usual SPH cubic spline interpolation kernel (dimensions of inverse volume) dependent on particle separation r_{ij} and mean smoothing length $h_{ij} = 0.5(h_i + h_j)$. x_i^α and v_i^α are respectively the α component of the position and velocity of particle i , and m_j stands for the mass of particle j .

For the momentum equation, we use the usual symmetric form which ensures local momentum conservation. We write Eq. (2) as

$$\frac{dv_i^\alpha}{dt} = \sum_{j=1}^N m_j \left(\frac{\sigma_i^{\alpha\beta}}{\rho_i^2} + \frac{\sigma_j^{\alpha\beta}}{\rho_j^2} \right) \frac{\partial W_{ij}}{\partial x_i^\beta}, \quad (17)$$

where $\sigma^{\alpha\beta}$ is the total stress tensor defined in Eq. (3). In order to treat shocks, we add to Eq. (17) the usual artificial viscosity term.

The expressions for the time evolution of the internal energy and deviatoric stress tensors involve the strain rate tensor Eq. (5) and the rotation rate tensor Eq. (7). The components of these tensors are easily obtained from

$$\rho_i \dot{\epsilon}_i^{\alpha\beta} = \frac{1}{2} \sum_{j=1}^N m_j \left[(v_j^\alpha - v_i^\alpha) \frac{\partial W_{ij}}{\partial x_i^\beta} + (v_j^\beta - v_i^\beta) \frac{\partial W_{ij}}{\partial x_i^\alpha} \right]. \quad (18)$$

In all the calculations reported here, we used the so-called Tillotson equation of state (Tillotson 1962, Benz et al. 1994). Although the code can handle an arbitrarily complicated equation of state, the Tillotson equation is sufficiently simple that almost no computing effort is spent on the equation of state. All relevant parameters for this equation of state for several geologically interesting rocks can be found in Asphaug and Melosh (1993). Finally, we note that, because in brittle material like rocks fracture cuts tensile stresses before they become large, we are not subject to any of the instabilities associated with large tensile stresses recently pointed out by Swegle et al. (1993).

4.2. Neighbor finding

Experiments have shown that to resolve fragments and cracks, a large number of particles have to be used, raising the computational costs of these simulations. As in any SPH codes, a large fraction of the computing time is spent finding the neighbors within the interaction length of the smoothing kernel. Thus, a fast search algorithm is required for the method to be of any use.

In absence of self-gravity, linked lists (Hockney and Eastwood 1981) are the fastest schemes available. Unfortunately, they suffer from two major problems: (i) they limit the space in which the calculation can be done and (ii) they become rapidly useless if particles have significantly different interaction lengths. The first limitation

comes from the fact that the so-called head-of-chain mesh is three-dimensional and extends $N_{\text{mesh}} * \delta$ along each direction where δ is the linear size of a cell (in practice the interaction length). Clearly, since memory requirement scales like N_{mesh}^3 , large values of N_{mesh} are impossible, thus effectively limiting the spatial extent of the simulations. The second limitation comes from the fact that for widely varying particle sizes (factor 3–5) δ becomes poorly defined. Linked lists are therefore usually replaced by hierarchical tree methods (see for example Benz et al. 1990) even though self-gravity is not needed. Here we propose an alternate scheme based on linked lists that does not suffer from the disadvantages pointed out above.

The essence of our scheme is to build linked lists in rank space instead of in real space. To achieve this, we first rank the particles along each of the three axis. If $r_{x,i}, r_{y,i}, r_{z,i}$ are the ranks of particle i along the x , y and z -axis respectively, linked lists can be built by assigning particle i the following address k, l, m in the rank space mesh:

$$k = \frac{r_{x,i}}{N_{\text{cell}}}, \quad l = \frac{r_{y,i}}{N_{\text{cell}}}, \quad m = \frac{r_{z,i}}{N_{\text{cell}}}, \quad (19)$$

where N_{cell} is a free adjustable parameter. A value for this parameter can be obtained by considering the following chain of arguments. For this scheme to work best, it is imperative that the filling factor of the mesh be roughly uniform and that only a few cells need to be searched to find all the neighbors of a given particles. Since SPH uses on average around 50 neighbors per particle and that in a three-dimensional lattice every cell is surrounded by 26 neighboring cells, a filling factor of about 1–2 will be appropriate. For particles distributed randomly in space, we obtain an average filling factor of 1 if we set $N_{\text{cell}} = N_{\text{part}}^{2/3}$ where N_{part} is the number of particles. The rest of the algorithm proceeds in an identical manner to the more conventional linked lists. The only additional requirement is a mapping between rank space and real space. This mapping can be obtained by storing the actual spatial extent along all three axes of each cell in the rank mesh. The numbers of rank space cells to be opened along each of the axes in a neighbor search can be

determined by comparing the smoothing length to the sizes of the cells on either side of the particle under consideration. Finally, to make sure that no neighbors are missed, we access the particles sequentially in descending order of interaction length, making use of the symmetry in all SPH expressions.

Our scheme does not limit the spatial extent of the simulations since the linked lists are constructed in rank space and that the memory requirement to store the three-dimensional rank mesh is just of order N_{part} (for $N_{\text{cell}} = N_{\text{part}}^{2/3}$). This scaling can be understood from the fact that in rank space the mesh is built while trying to minimize the number of empty cells, the ideal mesh being one with only about 1 to 2 particles per cell. This is quite contrary to the mesh usually built in real space which is very sparse. In addition, the sorting required to rank the particles, which normally scales like $N_{\text{part}} \log(N_{\text{part}})$, can be made faster as particles remain quasi-ordered from one timestep to the next.

4.3. Fracture

The implementation of fracture in our SPH code begins by assigning, as part of the initial conditions, N_f crack activation threshold strains to the body. These thresholds are distributed in a uniformly random manner among all the particles until each has been assigned at least one flaw. For each flaw j , $1 \leq j \leq N_f$, a particle i is chosen at random and attributed the corresponding activation threshold derived from the Weibull distribution (Eq. (11)):

$$\epsilon_{i,j}^{\text{act}} = \left[\frac{j}{kV} \right]^{1/m}. \quad (20)$$

The total number of flaws required to assign at least one flaw to each of N_{part} particles is, on average, $N_f \approx N_{\text{part}} \ln(N_{\text{part}})$, if they are chosen with replacement so as to ensure a uniformly random distribution. Because this is not a consecutive assignment of flaws, a given particle can receive several n_i^{tot} flaws with a wide range of activation thresholds. When a particle feels a strain ϵ_i greater than any of these activation thresholds, fracture begins.

Notice that by changing the seed of the random number generator, the location of any specific activation threshold is changed while the overall distribution remains the same. Thus simulations differing only by the seed of the random number generator will have the location and sizes of fractures and fragments scattered around a common mean. This scatter is well known to experimentalists as even when great care is taken to reproduce twice the same fracture experiment, results always differ by some measure.

In multi-dimensions, ϵ_i is computed from the maximum tensile stress σ_i^t (possibly already reduced by damage and yielding) after a principal axis transformation (Melosh et al. 1992). The local scalar strain ϵ_i is then obtained from the relation

$$\epsilon_i = \frac{\sigma_i^t}{(1 - D_i)E}, \quad (21)$$

where D_i is the local value of the damage, E is Young's elastic modulus of the undamaged material in uniaxial stress, $E = 9K\mu/(3K + \mu)$, and K is the bulk modulus. Young's modulus is chosen to ensure that the system reduces to its 1D form in uniaxial stress events.

If ϵ_i exceeds any of the flaw activation thresholds $\epsilon_{i,j}^{\text{act}}$ contained in particle i , damage associated with particle i accumulates at a rate given by Eq. (15) multiplied by the number n_i of active flaws inside the particle. Damage is allowed to accumulate to a maximum value given by

$$D_i^{\max} = \left(\frac{n_i}{n_i^{\text{tot}}} \right)^{1/3}, \quad (22)$$

where n_i^{tot} is the total number of flaws inside particle i . Clearly, a necessary condition for a given particle to reach a totally damaged state (i.e. unable to sustain any tensile or shear stresses) is that all internal flaws are activated. Note that the average number of flaws contained per particle is $\langle n_i^{\text{tot}} \rangle \approx \ln(N_{\text{part}})$, or ~ 12 for a 10^5 particle simulation.

4.4. Search for fragments

Once fracture has ceased in the target, we search for contiguous regions of undamaged par-

ticles and call them fragments. A fragment is therefore a volume of neighboring particles which are still connected by strength, and bounded by a strengthless (or empty) region. The identification of fragments is done as a part of the post-processing. At first, it may appear that identifying fragments should not be a difficult task but this is not the case. The problem comes from the fact that the simulation can not be carried out to late enough time (due to the explicit nature of the code) for the fragments to become well-separated in space. Therefore, we need to be able to identify fragments *before* they have significantly moved away from one another. We have devised a two-step method that has proven to be quite successful.

First, we anticipate the ultimate state of fragmentation (the answer we would get given unlimited hydrodynamical evolution of the target) by processing undamaged particles in the following manner: We compute the principal tensile axis of the stress tensor, as before, and if this value exceeds the static failure strength of the rock the particle is assigned a damage $D = 1$. (The static failure strength is used because these last fracture events occur at relatively low strain rates.) We then identify fragments using a friends-of-friends algorithm; we start with any undamaged particle and search for any undamaged neighbors (a neighbor is defined by a particle within one smoothing length). The next step consists of finding the undamaged neighbors of the undamaged neighbors, and so on, until no more particles can be added to the fragment. Each particle that belongs to the fragment is removed from the list of available particles, and the search for another fragment can begin. The procedure stops when no more undamaged particles are available.

Because in SPH the interaction range goes beyond the nearest neighbor out to $2h$, it actually takes at least two totally damaged particles (for equally spaced particles $\sim h$ apart) between two undamaged ones to zero out all tensile forces between the latter two. For this reason, we include in our fragment-finding algorithm the first layer of adjacent damaged particles. However, neighbors for these particles are not searched. Hence, our final fragments are made out of un-

damaged particles coated with a veneer (one layer thick) of $D = 1$ particles.

5. Tests

We performed a large number of tests in order to check all aspects of the code. These included finding equilibrium solutions of deformed solid beams, checking for the correct propagation of elastic waves, simulating the bouncing of tennis balls, computing the growth of a single crack, and comparing numerical results with various laboratory impact experiments. To illustrate the capabilities of our method, we present in this section the results of three different tests: the cracking of a rod under tension, the catastrophic disruption of a basalt sphere by impact, and a half-space cratering event into San Marcos gabbro.

5.1. A tensile rod

The accuracy of our model depends upon the realistic propagation of explicit cracks, so we must ensure that these cracks propagate in a manner consistent with dynamic fracture physics. Principally, we must show that flaws nucleate as expected from the Weibull distribution, and that once nucleated, they grow orthogonal to the applied stress with the crack growth velocity c_g and that the resulting fracture pattern has the experimentally observed rate dependency. We shall demonstrate this with two examples of a cylindrical rod undergoing dynamically increasing (yet equilibrated) longitudinal extension. In each case the specimen is a basalt cylinder 1 cm in radius and 4 cm in length, represented by about 50 000 smooth particles. The difference between these two examples lies in the tension applied at both ends of the cylinders which translates into a factor of 6 difference in strain rate between the two.

Snapshots taken at various times during the simulation of the first low-strain-rate rod are shown in Fig. 1. Cracks first nucleate at a number of sites more or less independently as the weakest flaws of the Weibull distribution are activated. As the strain increases, cracks organize and grow along paths of least resistance given the far-field

stress. The results are jagged fractures propagating nearly perpendicular to the applied stress field. The speed at which one of these cracks propagate was found to be in very good agreement (within 5%) of the analytical crack growth velocity based on the longitudinal sound speed. This is also the speed at which cracks grow within our particles, at the micro-scale, so that resolved and unresolved cracks propagate at the same rate. Unresolved cracks relieve stress according to Eq. (15), whereas resolved cracks such as are shown here relieve stress by the actual fracturing of bonds and the opening of new free surfaces.

In Fig. 2 we compare the final outcome of two simulations differing by a factor of 6 in the actual tensile loading rate applied. Clearly, the simulation with the high strain rate appears to develop a significantly larger network of cracks in good agreement with experiments.

5.2. Laboratory impact experiments on basalt spheres

We have chosen to simulate the laboratory impact experiments on basalt spheres by Nakamura and Fujiwara (1991), as these experiments provide us not only with the final fragment mass spectrum but also with information on the dynamics of the debris (velocities, rotation rates, etc.) and fragment shapes. In these experiments, a small ≈ 0.2 g nylon bullet impacts a 3 cm radius basalt sphere off-axis at ≈ 3.2 km/s. Different experiments correspond to different impact parameters as measured by the impact angle α of the projectile with respect of the local normal to the surface. For a more detailed comparison between simulations and laboratory experiments see Benz and Asphaug (1994).

The evolution of an $\alpha = 30^\circ$ impact during the first few tens of microseconds is illustrated in Fig. 3. A total of 95 000 particles have been used to simulate this impact, 93 000 in the target and 2 000 in the projectile (not shown here). These snapshots illustrate clearly the manner in which damage grows inside the target as a result of the impact. In general terms, damage proceeds initially in the tensile “tail” immediately behind the shock front. This tensile tail dies out as the shock

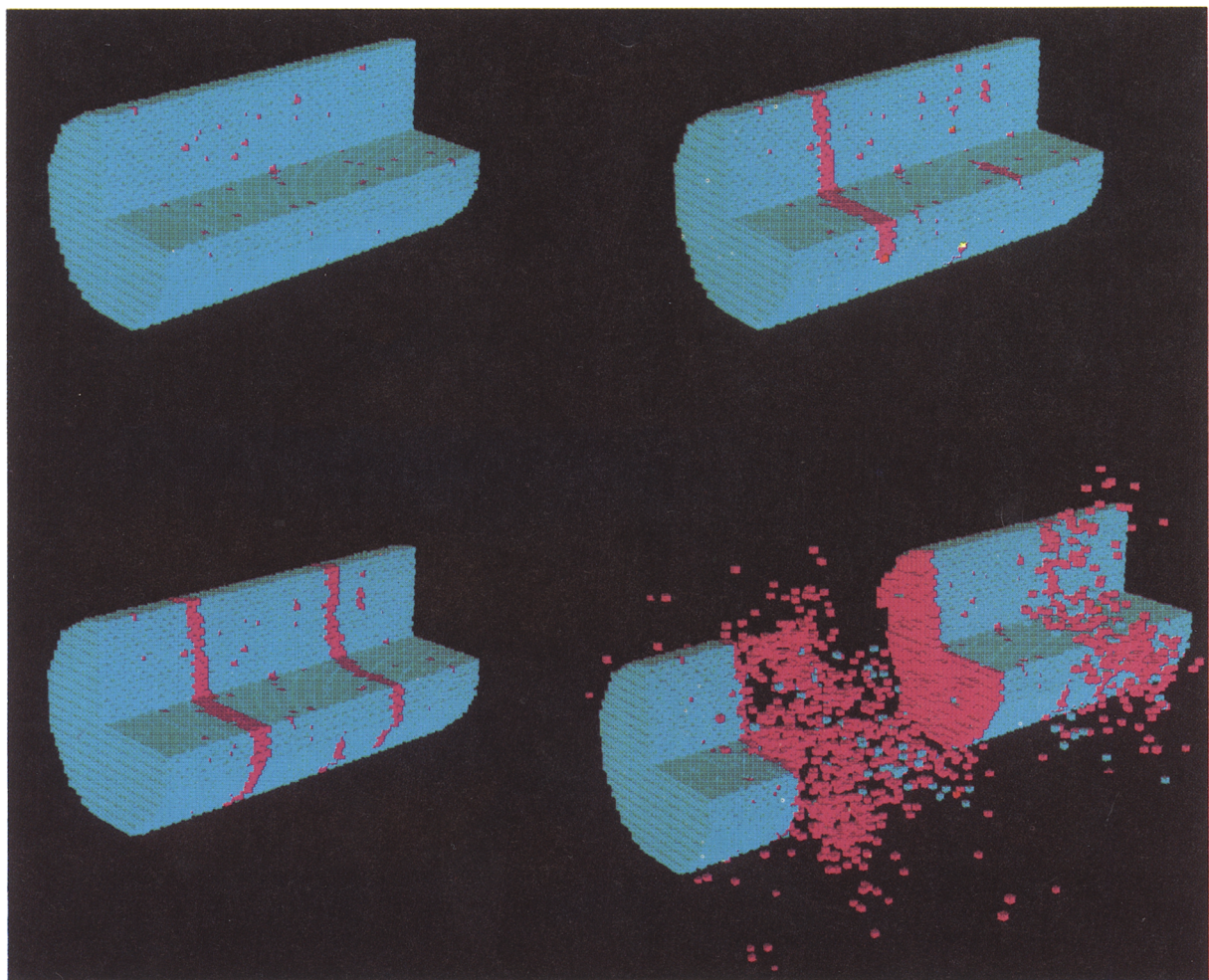


Fig. 1

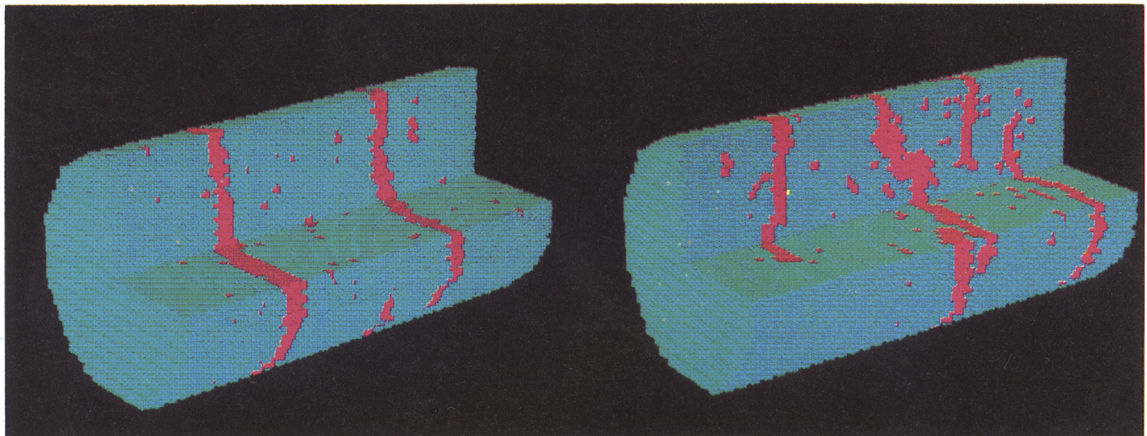


Fig. 2

weakens and becomes more linear; subsequent damage is the result of spallation stresses which form when compressive waves encounter a free surface and reflect back as tensile images. The first type of fracture is radially symmetric about the impact point and highly localized; the latter works its way around the surface of the target.

The region close to the impact point experiences the largest tensile strains and as a result is entirely broken into pieces smaller than what we can resolve. As we move away from the impact point, fracture proceeds mainly by forming cracks running beneath the surface. Eventually, these cracks surround the central region, shielding it from subsequent damage by preventing the transmission of tensile or shear waves to the interior. This shielding process naturally results in the formation of a nearly spherical core whose mass can be quite substantial. In the present simulation, the core mass is found to be $\approx 35\%$ of the target's mass compared to the 31% experimental value. The other sizeable fragments are essentially spalls whose masses are substantially smaller. As can be seen in Fig. 4, which represents the system at late time and in which fragments have been identified according to Subsection 4.4, the second largest fragment turns out to be a spall originating from the side of the target almost diametrically opposed to the impact point. These results are "robust" in the sense that very similar results are obtained for different initial random flaw distributions or even when reducing the number of particles by a factor 2.

5.3. Laboratory cratering experiments

Comprehensive experiments, particularly those which show the geometry of fracture in the rock, provide results at the level of detail necessary to adequately constrain current numerical modeling.

Not many experimentalists bother compiling or publishing such detailed data, primarily because the existing models have so far been unable to predict anything beyond crater diameter and fragment statistics.

In a recent paper, Ahrens and Rubin (1993) analyze hypervelocity impacts (5.2 km/s) of 0.143 g steel projectiles into 20 cm-sized cubes of Bedford limestone and San Marcos gabbro. These impacts induce fracture inside the target at distances far from the vicinity of the crater. They map the fracture geometry by making polished cross-sections through the final target. They subsequently analyze the extent of impact-induced fracture, as a function of distance r to the impact point, by cutting the targets into 1 cm cubes and measuring compressional wave speed in each of them. Because fracture damage reduces the elastic constants, wave speed (see below), becomes a quantitative instrument to assess the extent of damage in the rock. The elastic constants, sound speed and density for unfractured San Marcos gabbro were reported in an earlier paper by Lange et al. (1984), and for shock behavior we use the Tillotson equation of state for gabbroic anorthosite (Melosh 1989). Because of large experimental uncertainties in the values of m and k (Lange et al. (1984) report $m \approx 9$, whereas Ahrens and Rubin (1993) report $m \approx 3$), we performed a number of simulations in which we chose $m = 3, 6$ and 9 , and varied k so as to achieve best agreement with the data. Most runs used 80 000 particles, although in several runs we reduced N to 45 000 to test the robustness of the results to changes in resolution.

Fig. 5 is a 3D surface plot with a quadrant of the target removed that shows the results of our model for the value of $m = 3$ and $k = 1.39 \times 10^{12}$ resulting in the best match to the overall appearance of the fracture pattern. It is quite evi-

Fig. 1. Crack growth in an inhomogeneous tensile rod 4 cm long. Colors indicate location of damaged regions and a section of the rod has been removed to show internal structure. Notice that cracks first nucleate at random sites before organizing into a major fracture.

Fig. 2. Comparison between two tensile rods different in a factor 6 in the actual load applied. Notice that a higher loading rate (rod on the right) results in more numerous fractures.

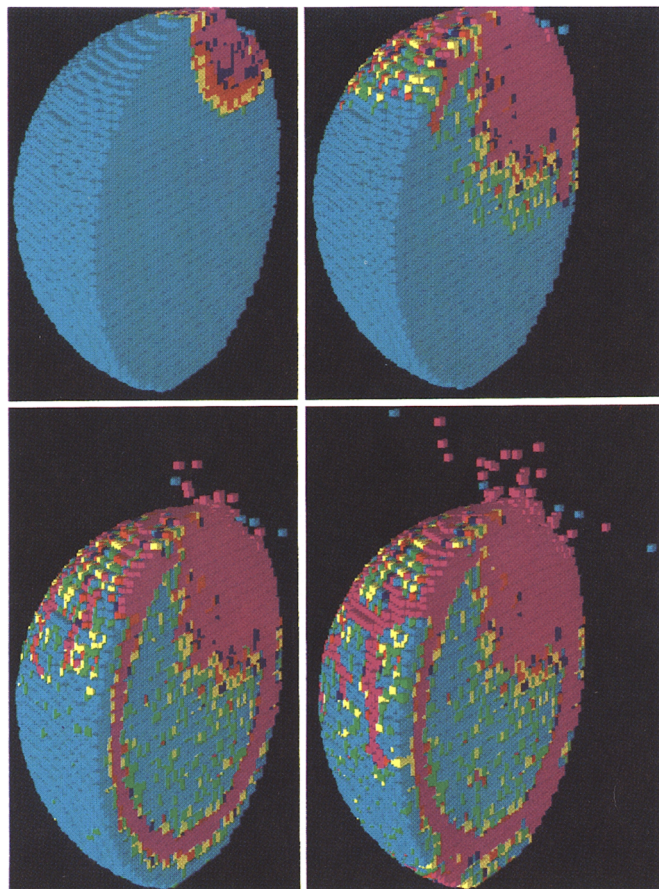


Fig. 3

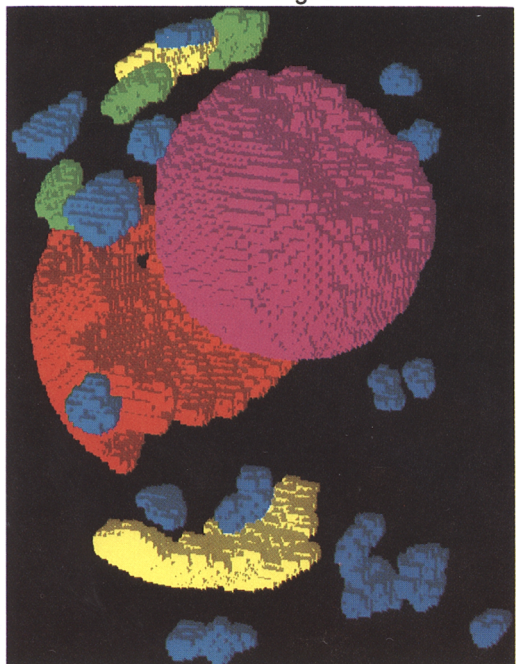


Fig. 4

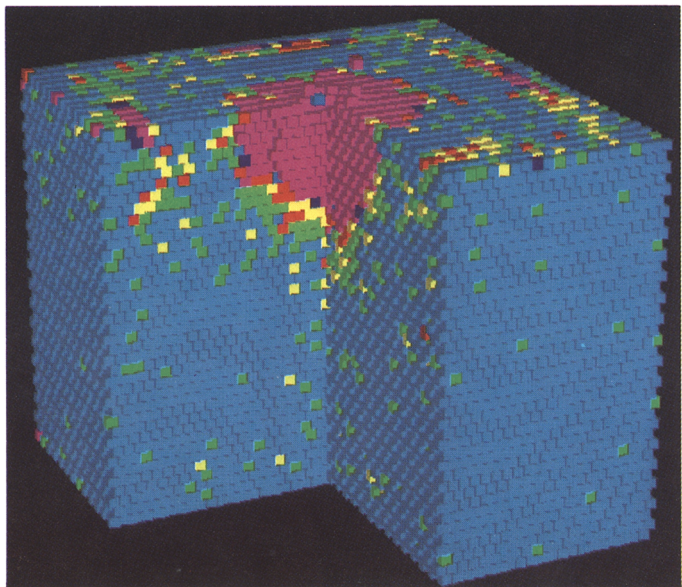


Fig. 5

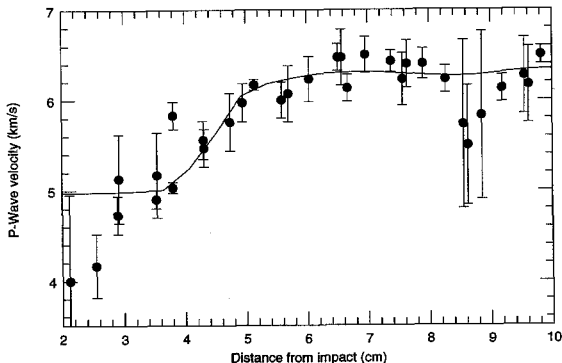


Fig. 6. Compressional wave speed as a function of distance to impact points. Solid dots represent laboratory values whereas the results of our simulations are indicated by the solid line.

dent that extensive damage to the target has occurred even at distances far beyond the immediate vicinity of the impact. Besides the heavily damaged central regions, the most striking features are the spall fractures near the edges of the target, the near surface fracture running horizontally and the radial fractures extending from the central heavily damaged regions.

The level of agreement between our simulations and the experimental data is made more quantitative in Fig. 6 in which we compare compressional wave speeds. Note that in the central, severely damaged regions as well as in the side fractures the experimentally-determined wave speed is significantly lower than in the one obtained in the simulations. This apparent discrepancy comes from the fact that the numerical wave speed is *not* a measured speed but is derived from the relation between damage and wave speed $c_p = \sqrt{[K + 4\mu(1 - D)/3]/\rho}$. Therefore,

the numerical determination does not, at the sub-particle scale, take into account the opening of voids and the corresponding decrease in bulk modulus.

As a consequence, the critical region in which to assess the realism of the simulation is the transition zone, centered around $r = 4$ cm. This region demarks the boundary of the crater, not so much in terms of its final size (the number most often reported in the experimental literature) but in terms of how cracks have propagated into the half-space. A number of numerical and analytical models can express the final crater diameter in terms of impact velocity or energy, but to fully understand the cratering process one needs a model capable of describing the transitions which occur along the boundary, particularly if one is eventually going to study complex craters which are reshaped by planetary gravity. For $m = 9$ and $m = 6$ we are unable to fit the damage profile across the crater, whereas our best-case test with $m = 3$ falls almost entirely within the spread of the measurements, as can be seen in the figure.

6. Conclusions

We have presented a model of materials with strength in the framework of smooth particle hydrodynamics (SPH). We use Hooke's law to compute the non-diagonal terms of the stress tensor, which are then modified by a von Mises yielding relation for stresses beyond the elastic limit. For the lower stresses associated with brittle failure, we developed a new fracture model based on the nucleation of incipient flaws whose

Fig. 3. 3D surface plots of the target at 5, 10, 25, 40 μ s (left to right and top to bottom) after impact for an angle of incidence of $\alpha = 30^\circ$. Again, color represents damage and the target is split in half along the symmetry plane to reveal the core.

Fig. 4. Late time fragments. Fragments have been identified using the procedure outlined in the text and colored according to the logarithm of their mass. Notice the large almost spherical core in the middle of the debris cloud as well as the large spall plate in the back.

Fig. 5. 3D plot of the target with a quadrant removed to show internal structure. Color represents damage ranging from light blue for undamaged rock; green, yellow and dark blue for increasingly fractured; and red for totally fractured (strengthless) material. Note that damage extends well beyond the immediate vicinity of the impact point as well as the large spall fractures near the edges of the target.

number density is given by a Weibull distribution. Our model of dynamic fragmentation explicitly reproduces the growth of cracks in a brittle elastic solid by rupturing bonds and forming new free surfaces. Cracks grow when local failure strains are exceeded, and stresses are relieved across the crack boundaries. The release of stress along fracture walls increases differential stress at the crack tips, driving cracks forward in the manner of an actual brittle solid. Tensile and shear stresses are unsupported across disconnected regions, leading to reduced average strength and sound speed (i.e. damage) in the body. By producing actual cracks and fragments, our method automatically takes into account friction between fragments and bulking, effects which are included as recipes in statistical damage models. Although the current version of our code only includes explicitly tensile failure, we are currently working on a version that will allow shear failure as well. These modes of failure are extremely important under compressive stresses such as those occurring in plate tectonics and giving raise to earthquakes.

Because micro-scale cracks within each smooth particle grow at the same rate as the macro-scale (explicit) cracks, our model represents a resolution-independent fracture physics. High resolution is required if one is to model sharp stress waves, shocks, and/or the formation of small fragments, but until the advent of resolution-independent fracture, hydrodynamical accuracy was limited by the fragmentation model, an issue we addressed earlier (Benz and Asphaug 1994). High resolution, particularly in 3D, makes our method more computer intensive than previous, purely statistical damage models, but it provides the invaluable advantage of modeling fragments explicitly. Thus, the usual recipes used to take into account fragment interactions (like bulking for example) are naturally taken into account on the scales resolved by the code. Furthermore, recent experiments in porting the smooth particle hydrodynamics method on massively parallel machines have shown that codes using 10^7 particles could be run on architectures such as the CM5.

We have checked all aspects of the code by performing a wide variety of tests. These include finding equilibrium solutions of deformed solid

beams, checking for the correct propagation of elastic waves, simulating the bouncing of tennis balls, etc. We have illustrated the capabilities of our fracture model by examining the propagation of a single crack in a simple tensile rod and by comparing simulations and laboratory experiments relative to high speed impacts and cratering. In all cases, the method reproduces laboratory experiments to a level of detailed accuracy never achieved before.

Acknowledgement

The work presented here has been supported in part by NASA grant NAGW-3904.

References

- Ahrens, T.J., and Rubin, A.M., 1993, J. Geophys. Res., **98**, 1185–1203.
- Asphaug, E., and Melosh, H.J., 1993, The Stickney Impact of Phobos: A Dynamical Model, Icarus **101**, 144–164.
- Benz, W., 1990, in: Numerical Modeling of Nonlinear Stellar Pulsation: Problems and Prospects, ed. J.R. Buchler, (Kluwer Academic, Dordrecht).
- Benz, W., and Asphaug, E., 1994, Icaros, **107**, 98–116.
- Benz, W., Ryan, E., and Asphaug, E., Numerical Simulations of Catastrophic Disruption: Recent Results, in: The 4th International Workshop on the Catastrophic Disruption of Small Solar System Bodies, Gubbio, Italy (1994).
- Benz, W., Bowers, R.L., Cameron, A.G.W., and Press, W.H., 1990, Dynamic Mass Exchange in Doubly Degenerate Binaries. I. 0.9 and 1.2 M. Stars, Astrophys. J., **348**, 647–667.
- Grady, D.E., and Kipp, M.E., 1980, Int. J. Rock Mech. Min. Sci. Geomech. Abstr., **17**, 147–157.
- Hockney, R.W., and Eastwood, J.W., 1981, Computer Simulation Using Particles (McGraw-Hill, New York).
- Jaeger, J.C., and N.G.W. Cook, 1969, Fundamentals of Rock Mechanics (Chapman and Hall, London).
- Lange, M.A., Ahrens, T.J., and Boslough, M.B., 1984, Icarus, **58**, 383–395.
- Lawn, B.R., and Wilshaw, T.R., 1975, Fracture of Brittle Solids (Cambridge Univ. Press, New York).
- Liberky, L.D. and Petschek, A.G., 1990, Smooth particle hydrodynamics with strength of materials, in: Advances in the Free-Lagrange Method, Trease and Crowley, eds., (Springer, Berlin) p. 248.
- Lucy, L., 1977, Astron. J., **82**, 1013.
- Melosh, H.J., 1989, Impact Cratering: A Geologic Process, (Oxford Univ. Press, New York).

- Melosh, H.J., Ryan, E.V., and E. Asphaug, 1992, Dynamic Fragmentation in Impacts: Hydrocode Simulation of Laboratory Impacts. *J. Geophys. Res.* **97**, 14,735–14,759.
- Monaghan, J.J., 1992, Smooth Particle Hydrodynamics. *Ann. Rev. Astron. Astrophys.*, **30**, 543–574.
- Nakamura, A. and A. Fujiwara, 1991, Velocity Distribution of fragments Formed in a Simulated Collisional Disruption. *Icarus*, **92**, 132–146.
- Swegle, J.W., Hicks, D.L., and Attaway, S.W., 1993, Smoothed Particle Hydrodynamics Stability Analysis, in proceedings of Colloquium on Advances in Smooth Particle Hydrodynamics, Albuquerque, N.M., 21–23 January, pp. 185–207.
- Tillotson, J.H., 1962, Metallic equations of State for Hypervelocity Impact. General Atomic report GA-3216, July 1962.
- Weibull, W.A., 1939, A statistical theory of the strength of materials (transl.), Ingvetensk. Akad. Handl. (Stockholm) **151**, pp. 5–45.
- Wingate, C.A., and Fisher, H.N., 1993, Strength Modeling in SPHC, Los Alamos National Laboratory report, LA-UR-93-3942.